Uncovering the process that transports magnetic helicity to coronal mass ejection flux ropes

Pal, Sanchita

2022-09-15

Pal , S 2022 , ' Uncovering the process that transports magnetic helicity to coronal mass ejection flux ropes ' , Advances in Space Research , vol. 70 , no. 6 , pp. 1601-1613 . https://doi.org/10.1016/j.asr.202

http://hdl.handle.net/10138/347629
https://doi.org/10.1016/j.asr.2021.11.013

Available online at www.sciencedirect.com

ScienceDirect

Advances in Space Research 70 (2022) 1601–1613

ADVANCES IN SPACE RESEARCH
(a COSPAR publication)

www.elsevier.com/locate/asr

Uncovering the process that transports magnetic helicity to coronal mass ejection flux ropes

Sanchita Pal *

Center of Excellence in Space Sciences India, Indian Institute of Science Education and Research Kolkata, Mohanpur 741246, West Bengal, India
Department of Physics, University of Helsinki, P.O. Box 64, FI-00014 Helsinki, Finland

Received 6 August 2021; received in revised form 9 November 2021; accepted 14 November 2021
Available online 20 November 2021

Abstract

Magnetic helicity, an intrinsic property of eruptive helical flux ropes (FRs) forming coronal mass ejections (CMEs), plays an important role in determining CME geoeffectiveness. In the solar atmosphere and heliosphere, helicity remains conserved in a closed volume. Considering this fact as a basis of our study, we perform a quantitative comparison between total magnetic helicity and twisted flux in interplanetary CMEs and those transported to CMEs via magnetic reconnection at low corona. At the source, twisted/poloidal flux (ϕ_{pcme}) of CMEs is directly estimated from total reconnection flux, and CME helicity (H_{cme}) is obtained by combining reconnection flux information with CME physical parameters. At 1 AU, the twisted/poloidal flux (ϕ_{pmc}) and helicity (H_{mc}) of CMEs are obtained from in situ observations. Considering uncertainties steaming from FR length, reconnection flux and CME physical parameter estimations, poloidal flux and helicity of CMEs at 1 AU are found to be highly relevant ($\frac{\phi_{pmc}}{\phi_{pcme}} = 0.4$–$1.5$, $\frac{H_{mc}}{H_{cme}} = 0.3$–$1$) to low-corona magnetic reconnection at the wake of CMEs. This result remains unchanged despite CME association with pre-existing FRs. We show that a significant reduction in CME helicity during its heliospheric propagation may result from a high rate of FR erosion in the interplanetary medium. Our event analysis confirms that CME's intrinsic magnetic properties are transported to CME FRs during magnetic reconnection at sheared coronal arcades. A one-to-one correspondence between the chirality of 1-AU CMEs and their pre-eruptive structures complies with the fact that the sense of field line rotations in FRs may remain unchanged during coronal reconnection at the source. By connecting intrinsic magnetic properties of FRs through Sun-Earth medium, this study provides important implications for the origin of geoeffectiveness in CMEs.

Keywords: Coronal mass ejection; Magnetic reconnection; Interplanetary magnetic field; magnetic cloud; Flux rope

1. Introduction

A twisted bundle of magnetic field lines is known as magnetic flux rope (FR). The most prominent manifestation of solar activity is FRs being ejected from the Sun (Low, 1996) carrying a substantial amount of magnetized coronal mass in the interplanetary medium. These eruptive magnetic FRs majorly form coronal mass ejections (CMEs; Webb and Howard, 2012; Vourlidas et al., 2013) which are observed as bright dynamic structures in coronagraphs. The FR structures of interplanetary CMEs (ICMEs) represent magnetic clouds (MCs) manifesting themselves by smoothly rotating magnetic field vectors, strong magnetic field intensity, low plasma$-\beta$, and low ion temperature than the ambient solar wind (Burlaga et al., 1981; Lepping et al., 1990; Lepping et al., 1997) in situ observations. However, FRs are not always observed in ICMEs because of CME deformations due to interaction with ambient solar wind (Odstrcil and Pizzo, 1999; Savani

* Address: Department of Physics, University of Helsinki, P.O. Box 64, FI-00014 Helsinki, Finland.
E-mail address: sanchita.pal@helsinki.fi.

https://doi.org/10.1016/j.asr.2021.11.013
0273-1177/© 2021 COSPAR. Published by Elsevier B.V.

et al., 2010) or other CMEs (Burlaga et al., 2002; Manchester et al., 2017), CME erosion due to reconnection with interplanetary magnetic fields (IMFs; Ruffenach et al., 2015; Pal et al., 2020) and spacecraft crossing path being through ICME legs or far from their centers (Cane et al., 1997; Kilpua et al., 2011).

Often eruptive FRs are observed to have associations with solar filaments or prominences (Bothmer and Rust, 1997; Crooker, 2000), extreme ultra-violet (EUV) and/or soft X-ray dimmings (Rust, 1983; Sterling and Hudson, 1997), X-ray sigmoid structures (Rust and Kumar, 1996; Canfield et al., 1999; Leamon et al., 2004) and solar flares (Youssef and Mawad, 2013; Schmieder et al., 2015). The studies by Georgoulis et al. (2019), Patsourakos et al. (2020) have discussed pre-eruptive magnetic field configuration of CME FRs in detail. The solar origin and formation of local FRs have been studied using numerous models for decades. Few suggest that FRs emerge from below the solar surface (Low, 1994; Fan and Gibson, 2004), Other consider the formation of FRs at low corona due to gradual processes like slow reconnection and flux transport (Mackay and Van Ballegooijen, 2001). Some studies find the reason behind FR eruptions being the loss of equilibrium (Forbes and Priest, 1995; Lin et al., 2004) and/or presence of magnetic reconnection that opens up the overlying flux and allows core FR to penetrate the overlying field lines (Sturrock, 1989; Lynch et al., 2004). In this case, the FRs are pre-existing. Few studies suggest that FRs form due to magnetic reconnection at sheared magnetic arcades during the eruption (Moore and Labonte, 1980; Antiochos et al., 1999; Choe and Cheng, 2000). An observational analysis of CME solar sources by Dere et al. (1999) suggested that the formation of FRs occurs during an eruption. Based on a comparison of magnetic flux budgets in MCs and associated CMEs Qiu et al. (2007) suggested that low coronal reconnection is responsible for forming twisted FRs. Démoulin et al. (2002), Nindos and Zhang (2002) compared the magnetic helicity budget in MCs and pre-eruption solar sources and inferred that helical FR of CMEs forms during eruption rather than before the ejection of CMEs.

Magnetic helicity represents twist, link, and whirl in magnetic flux tubes in a closed volume (Pevtsov et al., 2014). It remains conserved in the solar atmosphere and heliosphere Berger and Field (1984). Also, in a force-free magnetic field configuration such as FRs, total magnetic helicity is conserved (Woltjer, 1958). Therefore, magnetic flux and helicity remain invariant throughout the interplanetary propagation if FRs do not erode significantly. Dasso et al. (2006), Ruffenach et al. (2012), Ruffenach et al. (2015), Pal et al. (2020) observed substantial magnetic flux erosion in MCs due to reconnection with ambient IMFs. By analyzing the radial twist distribution of two MCs, of which one was found to be significantly eroded and another had a little erosion, Pal et al. (2021) showed that erosion could peel off the twisted envelope of MCs. Some studies performed quantitative comparisons between magnetic properties, specifically magnetic flux and helicity of MCs and those of progenitor filaments (Lepping et al., 1997), coronal dimming (Webb et al., 2000; Mandrini et al., 2005), and source active regions (Leamon et al., 2004). Moreover, these comparative analyses have been the basis of several studies that aim to study the eruptive FR formations and the processes by which solar magnetism is transferred in them (Dasso et al., 2005; Qiu et al., 2007; Cho et al., 2003; Hu et al., 2014).

Nandy (2006) performed photospheric observation of magnetic flux tube helicity manifested by twist and writhe of solar active regions and suggested that flux tubes have a wide range of twists which can constrain their formations and dynamics in the solar convection zone. Démoulin et al. (2002) calculated the helicity injected by differential rotation at the photospheric level, the helicity of coronal magnetic field lines by fitting the soft X-ray loops with models, and the helicity of MCs. This study found that the coronal field helicity and the helicity of MCs are a factor of 2.5–4 and 4–20 larger than that provided by differential rotation, respectively. Nindos et al. (2003) measured the helicity injected in solar active regions due to transient photospheric horizontal flows and flux emergence using the local correlation tracking (LCT) method and compared the helicity values with those of MCs. The study found that the injected helicity into the corona is a factor of 2.9–4 lower than the total MC helicity. Furthermore, these studies calculated the MC helicity to estimate the helicity that could be shed via CMEs.

Pal et al. (2017) devised a method of estimating helicity in CMEs at 10 R_s radial distance from the Sun, assuming CMEs as cylindrical force-free configurations. The method requires FR's axial field strength and few FR physical parameters such as its cross-sectional radius and length. Gopalswamy et al. (2017) formulated a convenient technique named "flux rope from eruption data" (FRED) to derive the magnetic field intensity of FRs using post-eruption arcades (PEAs) frequently formed at solar sources of eruptive FRs. In the lower corona, PEAs are observed in both EUV (Tripathi et al., 2004) and soft X-ray observations (McAllister et al., 1996). The helicity of FRs in the interplanetary medium, mostly at 1 AU, had been estimated by several studies like Démoulin et al. (2002), Lynch et al. (2004) and Pal et al. (2017). Dasso et al. (2005, 2007) measured helicity in MCs using a method called the "direct method" that uses in situ solar wind magnetic field and velocity data in FR frame, rather than any prior estimation of MC structure. Also, the method has been used to calculate the eroded magnetic flux and helicity in MCs (Ruffenach et al., 2015; Pal et al., 2020; Pal et al., 2021).

The knowledge of magnetic helicity sign, i.e., chirality that represents the sense of twist of FRs (right-handed or left-handed) is required in the determination of field pattern in CMEs (Bothmer and Schwenn, 1998; Mulligan et al., 1998; Palmerio et al., 2017). The intrinsic magnetic structure of FRs plays a pivotal role in the space weather forecasting process. The strength and duration of an ICME FR's north–south magnetic field component measured in geocentric solar ecliptic (GSE) coordinate system determines the CME's geoeffectiveness. As there are no practical methods available for estimating three-dimensional coronal magnetic fields, thereby the magnetic structure of CMEs, several morphological patterns of eruptive events associated with CMEs and their sources are used as proxies of CME chirality (Marubashi, 1986; McAllister et al., 2001). Palmerio et al. (2017) studied the chirality of twenty FRs at 1 AU by applying minimum variance analysis (MVA; Sonnerup and Cahill, 1967) and at their sources using X-ray and EUV observations of associated pre-eruptive structures. They found a one-to-one correspondence between FR chirality at the source and in the interplanetary medium. Leamon et al. (2004) could not find any statistically significant sign and amplitude relationships between interplanetary FRs and associated source ARs. Based on observations, Winslow et al. (2016) inferred that reconnection between CME front and heliospheric plasma sheet (HPS) magnetic field in the interplanetary medium can significantly change the overall magnetic topology of ICME FRs.

By considering the conservation of magnetic helicity and flux as a basis of our study, we compare FR magnetic properties at source and 1-AU, and based on the comparison results, we discuss twisted FR formation at solar sources and how magnetic properties are transported to FRs. For this purpose, we select eleven events that have individual correspondence between CMEs and MCs and compare the helicity and flux of MCs at 1 AU with those of associated CMEs near the sources. Section 2 provides the overview of events, Section 3 explains the methodology used in this study, and Section 4 shows the results. Finally, in Section 5 and 6, we discuss and conclude our study.

2. Event overviews

To compare magnetic properties of FRs in Sun-Earth domain, we select eleven MCs from Richardson and Cane (2010) ICME catalogue (http://www.srl.caltech.edu/ACE/ASC/DATA/level3/icmeTable 2.htm) and HELCATS (https://www.helcats-fp7.eu/catalogues/wp4_icmecat.html). We follow Zhang et al. (2007) and Pal et al. (2017) to identify the progenitor CMEs. We utilise Hinode Flare Catalog (https://hinode.isee.nagoya-u.ac.jp/flare_catalogue/) and XRT Flare Catalog (https://xrt.cfa.harvard.edu/flare_catalog/) to identify associated flare with CMEs and AIA Filament Eruption Catalog (McCauley et al., 2015, https://aia.cfa.harvard.edu/filament/) to obtain CME association with filaments at their solar sources. The CME-MC pairs are selected based on the following criteria: (1) CMEs should be associated with post-eruption arcades (PEAs), (2) the magnetograms and EUV images of solar sources should be available, (3) near the Sun, CMEs should appear as clear FR structure simultaneously in multiple coronagraphs obtained from multiple viewpoints, (4) CMEs should not be preceded or followed by any other CMEs, and (6) throughout MC intervals both plasma and magnetic field in situ measurements should be available.

The methods employed in this study to analyze MCs require unambiguous identification of MC boundaries. We manually select each of their front and rear boundaries such that throughout the interval, solar wind parameters remain consistent with Burlaga et al. (1981) definition of MCs. In Table 1, we present a description of eleven events. In Column 1, we provide CME_{start}, when progenitor CMEs first appear in coronagraphs. The times are obtained from SOHO/LASCO Halo CME catalog (https://cdaw.gsfc.nasa.gov/CME_list/), Column 2 and 3 show the start time of associated flare ($flare_t$) and filament ($filament_t$) eruptions, Column 4 indicates the location of associated solar sources, Column 5 and 6 show the start (t_f) and end (t_r) times of corresponding MCs.

3. Methodology

In this Section, we describe procedures to derive magnetic properties of FRs in near-Sun and near-Earth domains.

3.1. Near-Sun CME magnetic properties estimations

We apply the FRED technique to obtain the magnetic properties of CMEs. The technique combines two key results - (1) the magnetic reconnection flux ϕ_{rc}, and (2) flux rope geometric properties. The reconnection flux represents photospheric magnetic flux under PEAs which map out the region of reconnection responsible for the formation of FRs during solar eruptions. The ϕ_{rc} is approximately equal to the poloidal flux of FRs near the Sun (Longcope and Beveridge, 2007). To measure ϕ_{rc}, we use PEAs and follow the procedure explained in Gopalswamy et al. (2017) and Pal et al. (2017). At first, the foot points of a full-grown PEA are identified on extreme ultra-violet (EUV) wavelength images like the 193 Å image obtained from Atmospheric Imaging Assembly (AIA; Lemen et al., 2011) instrument on board Solar Dynamic Observatory (SDO; Pesnell et al., 2011) spacecraft then the foot points are overlaid on the associated photospheric magnetograms. Here we use line-of-sight (LOS) magnetograms provided by Heliospheric Magnetic Imager (HMI; Scherrer et al., 2012) on board SDO. Finally, ϕ_{rc} is calculated using magnetic field intensity (B_{los}) available from magnetogram and the area of the region bounded by overlaid PEA foot points, following $\phi_{rc} = \frac{1}{2}\int_{PEA}|B_{los}|da$, where da is the elemental area. Pal et al. (2017) and Pal et al. (2021) show the measurement of ϕ_{rc} associated with Event 8 and 11 using above method, respectively. We determine 1-σ error in ϕ_{rc} by selecting PEAs for multiple times during the interval when they appear in full-grown structures in the solar EUV images. Estimation of ϕ_{rc} yields large uncertainties

Table 1
A description of events.

Ev No. (1)	CME_{start} (UT) (2)	$flare_t$ (UT) (3)	$filament_t$ (UT) (4)	source region (5)	t_f (UT) (6)	t_r (UT) (7)
1	2010/05/24 14:06	2010/05/24 13:05	–	S15W18	2010/05/28 20:46	2010/05/29 16:27
2	2011/05/25 13:25	2011/05/25 12:48	–	S18W20	2011/05/28 07:14	2011/05/28 20:12
3	2011/06/02 08:12	2011/06/02 06:31	–	S20E20	2011/06/05 01:50	2011/06/05 19:00
4	2012/02/10 20:00	–	2012/02/10 15:24	N35E25	2012/02/14 20:24	2012/02/16 05:34
5	2012/04/02 23:12	2012/04/02 21:53	–	N21E13	2012/04/06 11:31	2012/04/07 00:57
6	2012/06/14 14:12	2012/06/14 12:52	–	S19E06	2012/06/16 22:00	2012/06/17 14:00
7	2012/11/09 15:12	2012/11/09 14:45	–	S25E20	2012/11/13 08:23	2012/11/14 08:09
8	2013/03/15 07:12	2013/03/15 05:46	–	N11E12	2013/03/17 14:00	2013/03/18 00:45
9	2013/04/11 07:24	2013/04/11 06:55	–	N09E12	2013/04/14 16:41	2013/04/15 20:49
10	2013/06/02 20:00	–	2013/06/02 15:00	N15W22	2013/06/06 14:23	2013/06/08 00:00
11	2013/07/09 15:12	–	2013/07/09 14:15	N19E14	2013/07/13 04:39	2013/07/15 00:00

while PEAs appear far from the solar disk center because PEAs are observed as projected coronal structure on the solar disk.

Next, we obtain CME geometry including its aspect ratio (κ), half angular width (γ) by fitting it with a forward model technique named Graduated Cylindrical Shell (GCS) model (Thernisien et al., 2006) in multiple coronagraphs obtained from multi-viewpoint observations at a height $h = 10R_S$. We use C2 and C3 coronagraphs of Large Angle and Spectrometric Coronagraph (LASCO; Brueckner et al., 1995) telescope on board the Solar and Heliospheric Observatory (SOHO; Domingo et al., 1995) and COR2 A & B of Sun Earth Connection Coronal and Heliospheric Investigation (SECCHI; Howard et al., 2008) on board the Solar Terrestrial Relations Observatory (STEREO; Kaiser et al., 2008) to observe white-light CMEs. Fig. 1 and 5 of Pal et al. (2017) and Pal et al. (2018) show GCS model fitting on white-light CMEs associated with Event 6 and 8, respectively. From fitting results we estimate the height of CME legs $h_{leg} = h\, cos\gamma(1-\kappa)/(1+sin\gamma)$ (Thernisien et al., 2006), radius of CME arc $R_{arc} = \left(h - h_{leg}/cos\gamma\right)/2$, arc angle $y_{arc} = 2(\pi/2+\gamma)$ and CME cross-sectional radius $R_{cme} = h/(1+1/\kappa)$. Using h_{leg}, R_{arc} and y_{arc}, we derive the axial length of CME $L_{cme} = 2h_{leg} + y_{arc}R_{arc} - 2R_s$ (Pal et al., 2017). We find errors in estimating these parameters by considering an uncertainty of $\pm10\%$ in measuring CME geometry using GCS(Sarkar et al., 2020). In Column 2–5 of Table 2, we provide the geometric parameters like κ, γ, R_{cme} and L_{cme} of each event associated CMEs.

The poloidal flux $\phi_{p,cyl}$ and helicity H_{cyl} of a force-free cylindrical FR can be estimated following (Démoulin et al., 2002; Leamon et al., 2004; Lynch et al., 2004; Pal et al., 2017),

$$\phi_{p,cyl} = L\int_0^{R_{cyl}} \mathbf{B}_\phi \; rdr = \frac{L_{cyl}}{x_{01}} B_{cyl} R_{cyl}, \tag{1}$$

and

$$H_{cyl} = 4\pi L_{cyl}\int_0^{R_{cyl}} \mathbf{A}_\phi \mathbf{B}_\phi \; rdr \approx 0.7\; B_{cyl}^2 R_{cyl}^3 L_{cyl}. \tag{2}$$

Here $\mathbf{B}_\phi$ and $\mathbf{A}_\phi$ are poloidal component of magnetic field and vector potential, respectively. The parameters R_{cyl}, B_{cyl} and L_{cyl} are the radius, axial magnetic field intensity and length of cylindrical FRs. In Eq. 1, $x_{01} = 2.4048$ is the location of first zero of the nth order Bessel function, where $n = 0$. Approximating CMEs as force-free cylindrical FRs, their magnetic helicity H_{cme} can be computed following Eq. 2 (DeVore, 2000; Démoulin et al., 2002; Berger, 2003; Dasso et al., 2003; Lynch et al., 2004) using $R_{cyl} = R_{cme}, L_{cyl} = L_{cme}$ and $B_{cyl} = B_{cme}$. The CME magnetic field intensity B_{cme} can be found from Eq. 1 utilising $\phi_{p,cyl} = \phi_{rec}$.

Table 2
The physical properties of near-Sun (at 10 R_s) and near-Earth (at 1 AU) FRs.

Ev No. (1)	$\kappa \pm \delta_\kappa$ (2)	$\gamma \pm \delta_\gamma$ (°) (3)	$R_{cme} \pm \delta_{R_{cme}}$ (R_s) (4)	$L_{cme} \pm \delta_{L_{cme}}$ (R_s) (5)	R_{mc} (AU) (6)	B_{mc} (nT) (7)	p (8)	E_{rms} (9)
1	0.22±0.02	18±2	1.8±0.34	16.9±1.9	0.08	19	0.45	0.29
2	0.15±0.01	22±2.2	1.3±0.25	16.9±1.8	0.08	10.8	−0.13	0.52
3	0.15±0.02	17±2	1.3±0.25	16.9±1.8	0.03	29.2	0.56	0.28
4	0.23±0.02	25±2.5	1.9±0.35	17±2	0.15	9.5	0.15	0.36
5	0.21±0.02	17.3±2	1.7±0.32	16.9±1.9	0.07	17.3	−0.74	0.28
6	0.21±0.02	38±4	1.73±0.33	17±2.1	0.06	57.6	−0.14	0.2
7	0.2±0.02	18±2	1.7±0.32	16.9±1.9	0.11	24.2	−0.19	0.29
8	0.27±0.03	25.5±3	2.1±0.4	17±2	0.13	20.3	0.89	0.23
9	0.24±0.02	37±4	1.9±0.36	17.2±2.1	0.13	22.6	−0.85	0.16
10	0.21±0.02	18±2	1.7±0.33	16.9±1.9	0.18	14.3	−0.31	0.39
11	0.36±0.04	18±2	2.6±0.5	16.9±2	0.17	18.5	0.001	0.25

3.2. MC magnetic properties estimations at 1 AU

Near the Earth, MC's magnetic parameters are estimated by utilising in situ plasma and magnetic field data observed by Solar wind Electron, Proton and Alpha Monitor (SWEPAM; McComas et al., 1998) and Magnetic Field Experiment (MAG) instruments on board Advanced Composition Explorer (ACE; Smith et al., 1998) spacecraft. We employ linear force-free self-similarly expanding cylindrical flux rope model (Marubashi and Lepping, 2007) to least-squares fit the magnetic and plasma profiles of MCs. From the flux rope fit (FRF), we obtain MCs' geometry including its cross-sectional radius R_{mc}, magnetic field intensity B_{mc} and impact parameter p – the perpendicular distance between MC axis and spacecraft propagating path. Fig. 3 and 1 of Pal et al. (2017, 2021) demonstrate the least squares fit of linear force-free cylindrical model on magnetic and plasma profiles of MCs associated with Event 8 and 11, respectively. In Column 6–9 of Table 2, we provide R_{mc}, B_{mc}, p of eleven events studied here and the root mean square fitting errors E_{rms}, respectively. We compute poloidal flux ϕ_{pmc} and helicity H_{mc} of force-free cylindrical MCs using $B_{cyl} = B_{mc}, R_{cyl} = R_{mc}$ and $L_{cyl} = L_{mc}$, in Eq. 1 and 2. Here, B_{mc}, R_{mc} and L_{mc} are magnetic field intensity, cross-sectional radius and axial length of MCs, respectively.

The largest uncertainty in MC total flux and helicity estimations arises from MC axial length. Larson et al. (1997) derived L_{mc} as 2.5 AU by evaluating the travel time of supra-thermal electron propagation along field lines, DeVore (2000) found the MC axial length as $\pi/6 \approx 0.5$ AU by considering the longitudinal extension of CME as 30°. Démoulin et al. (2002) indicated the length as 2 AU, assuming that MCs are still rooted in the Sun while reaching at 1 AU. A statistical study by Démoulin et al. (2016) estimated L_{mc} as 2.6±0.3 considering the same fact that MCs are still attached to the Sun while they are observed at 1 AU. Nindos et al. (2003), Qiu et al. (2007) took the lower and upper limits of L_{mc} values as 0.5 and 2 AU in magnetic helicity and flux budget analysis. In this study, we consider the same limit of L_{mc} in MC's total flux and helicity estimations.

The magnetic flux and helicity of MCs suffer from erosion while they reconnect with ambient solar wind magnetized plasma. Reconnection creates an imbalance in flux measured in azimuthal plane – a plane formed by MC axis and spacecraft propagation path. This azimuthal flux imbalance can be captured in in situ observations if reconnected field lines remain attached to MCs. If reconnection occurs at MC front (rear), the reconnected field lines accumulate at its rear (front) and results in an imbalance in flux at its rear (front). From the flux imbalance information one can estimate MC's eroded flux and helicity, total flux and helicity before an ongoing erosion, and start time of ongoing erosion. Here we employ a technique called the 'direct method' (Dasso et al., 2006) that estimates the flux and helicity per unit length accumulated in FR azimuthal plane. Direct method utilises in situ magnetic field and plasma data transformed into cloud frame $(\hat{x}_{cloud}, \hat{y}_{cloud}, \hat{z}_{cloud})$ described in Dasso et al. (2006). To convert in situ data into cloud frame, the elevation and azimuth angles of MC axis are required. The angles can be obtained either by least-squares fit to MCs with models or by using minimum variance analysis (MVA) method, where the MVA intermediate variance direction corresponds to FR axis (Bothmer and Schwenn, 1998). Several studies like Ruffenach et al. (2012), Ruffenach et al. (2015), Pal et al. (2020), Pal et al. (2021) used direct method and estimated MC eroded flux and total flux before erosion. Applying this technique, we determine the time t_c when MC center crosses spacecraft. It corresponds to the time when absolute accumulated azimuthal flux attains its maximum value. Also, we estimate the time t_{im} when an imbalance in azimuthal flux begins. Once MC center is identified, the poloidal flux ϕ_y and helicity Hel per unit axial length L accumulated over in-bound (the path spacecraft travels during the interval $t_f - t_c$) and out-bound (the path spacecraft covers during $t_c - t_r$ interval) regions are determined as a function of coordinate x along the spacecraft propagation path perpendicular to the MC axis, where $x = 0$ corresponds to t_c. Thus,

$$\phi_y(x)/L_{mc} = \int_0^x B_{y,cloud}(x')dx' \quad (3)$$

and

$$Hel(x)/L_{mc} = 2\int_0^x B_{y,cloud}(x')\phi_z(x')dx', \quad (4)$$

where $\phi_z(x) = 2\pi\int_0^x B_{z,cloud}(x')x'dx'$, and $B_{y,cloud}$ and $B_{z,cloud}$ are azimuthal and axial field in cloud frame, respectively. If flux imbalance occurs at MC rear (front), total azimuthal flux, helicity before and after erosion are equal to $\phi_y(x_{be}), Hel(x_{be})$ and $\phi_y(x_{ae}), Hel(x_{ae})$, respectively, where x_{be} corresponds to t_r (t_f) and x_{ae} corresponds to t_{im}. We determine the time interval δt between the start of MC reconnection and MC observation at 1 AU following $\delta t = \frac{\tau_{exp} V_f}{V_{mc} - V_f}$, where $\tau_{exp} V_f$ represents the size by which the back (front) of MC expands since the start of reconnection at MC front (back) and $V_{mc} - V_f$ represents the relative velocity by which the rear (front) boundary gradually separates from MC if reconnection occurs at MC front (back). In Fig. 1a we plot ϕ_y per unit length along with $B_{y,cloud}$ as a function of time t of Event 1 MC. The times t_c and t_{im} are indicated on the plot by black and red dashed-dotted lines, respectively. In Fig. 1b and c, we plot ϕ_y/L_{mc} and Hel/L_{mc} of Event 1 as a function of x in in-bound and out-bound regions. The flux and helicity curves corresponding to in-bound and out-bound regions are shown in thin and thick lines, respectively. The FR is eroded at front and shows imbalance in azimuthal flux at its back. The firm black and dashed-dotted red vertical lines of Fig. 1b and c correspond to x_{be} and x_{ae}, respectively.

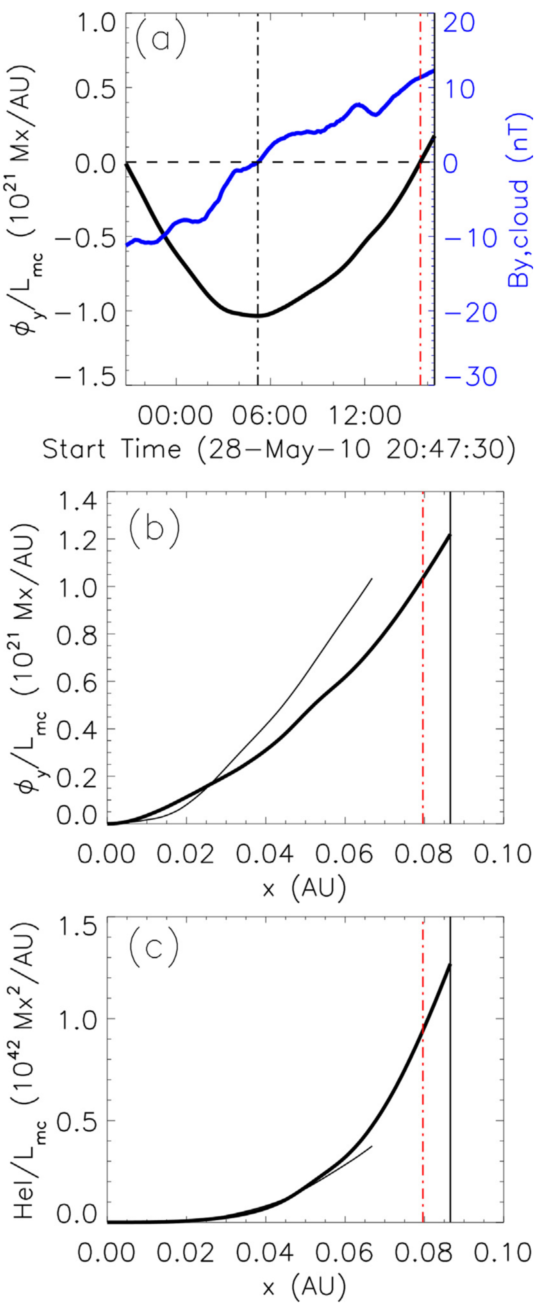

Fig. 1. Plots depicting (a) time evolution of ϕ_y/L_{mc} (black) and $B_{y,cloud}$ (blue) of Event 1 MC during its passage through spacecraft, (b) ϕ_y/L_{mc} and (c) Hel/L_{mc} in MC's in-bound (thin curve) and out-bound (thick curve) regions as a function of distance x from the MC center. The vertical dash-dotted black and red lines in (a) indicate t_c and t_{im}, respectively. The black and red vertical lines in (b) and (c) correspond to x_{be} and x_{ae}, respectively.

3.3. CME and MC chirality determination

To estimate the chirality or handedness of CME FRs, we analyse HMI/LOS magnetograms and multiple wavelength images of CME solar sources from SDO/AIA. The chirality of solar sources indicates the chirality of associated FRs as magnetic helicity is a conserved quantity even though magnetic reconnection is present (Berger, 2005). Palmerio et al. (2017) discussed several proxies to infer CME chirality near the Sun using solar source observations. The proxies utilised in this study are 1) Magnetic tongue (Fuentes et al., 2000; Luoni et al., 2011) – a vertical projection of the azimuthal component of emerging twisted flux tubes, where the right-handed (left-handed) chirality is indicated by the extension of leading (trailing) magnetic polarities under the southern edge of trailing (leading) magnetic polarities, 2) Dextral and sinistral natures of filament (Martin and McAllister, 1996; Martin, 2003), where the dextral (sinistral) filaments represent the negative (positive) chirality of associated CMEs, 3) EUV sigmoids – an S-shaped EUV configuration created by the field lines threading FR associated quasi-separatrix layers (Titov and Démoulin, 1999), where a forward (reverse) sigmoid structure is formed due to positive (negative) chirality of magnetic fields, 4) Skew of coronal arcades overlying the polarity inversion lines (PILs) (McAllister et al., 1995; Martin and McAllister, 1997) that represents the acute angle between the overlying coronal loops and associated PILs, where a coronal loop crossing over PIL in sense of a left-handed (right-handed) screw indicates negative (positive) chirality of associated CMEs (Martin, 1998), 5) Structure of 'J' shaped flare-ribbons (Démoulin et al., 1996), where a reverse (forward) 'J' corresponds to left-handed (right-handed) FR, and 6) Hemispheric helicity rule (Bothmer and Schwenn, 1998; Pevtsov and Balasubramaniam, 2003) that indicates negative (positive) helicity of FRs originating from Sun's northern (southern) hemisphere. The magnetic tongue is observed in SDO/HMI LOS magnetogram, whereas the filament nature, sigmoids, pre-erupting coronal arcades, and flare ribbons are observed in SDO/AIA 304, 131, 171 and 1600 Å, respectively. In Fig. 2, we show a few examples of determining CME chirality using proxies discussed above. The chirality of MCs at 1 AU is obtained utilizing two processes, 1) linear force-free cylindrical model fit to MCs and 2) MVA, where the direction of magnetic field rotation from intermediate to maximum plane is inspected to obtain MC chirality Palmerio et al. (2018).

4. Analysis and results

By applying the methods described in previous Section, we compute azimuthal/poloidal magnetic flux ϕ_{pcme} and ϕ_{pmc}, and helicity H_{cme} and H_{mc} of CMEs and MCs at a distance 10 R_s and 1 AU, respectively. This section compares the near-Sun and near-Earth FR helicity, chirality, and magnetic flux to investigate FR formation and transportation of magnetic properties in eruptive FRs.

4.1. Comparison of helicity and flux between 1-AU FRs and their solar sources

In Table 3, we provide FR magnetic properties along with their uncertainty values at 10 R_s and 1 AU in Column

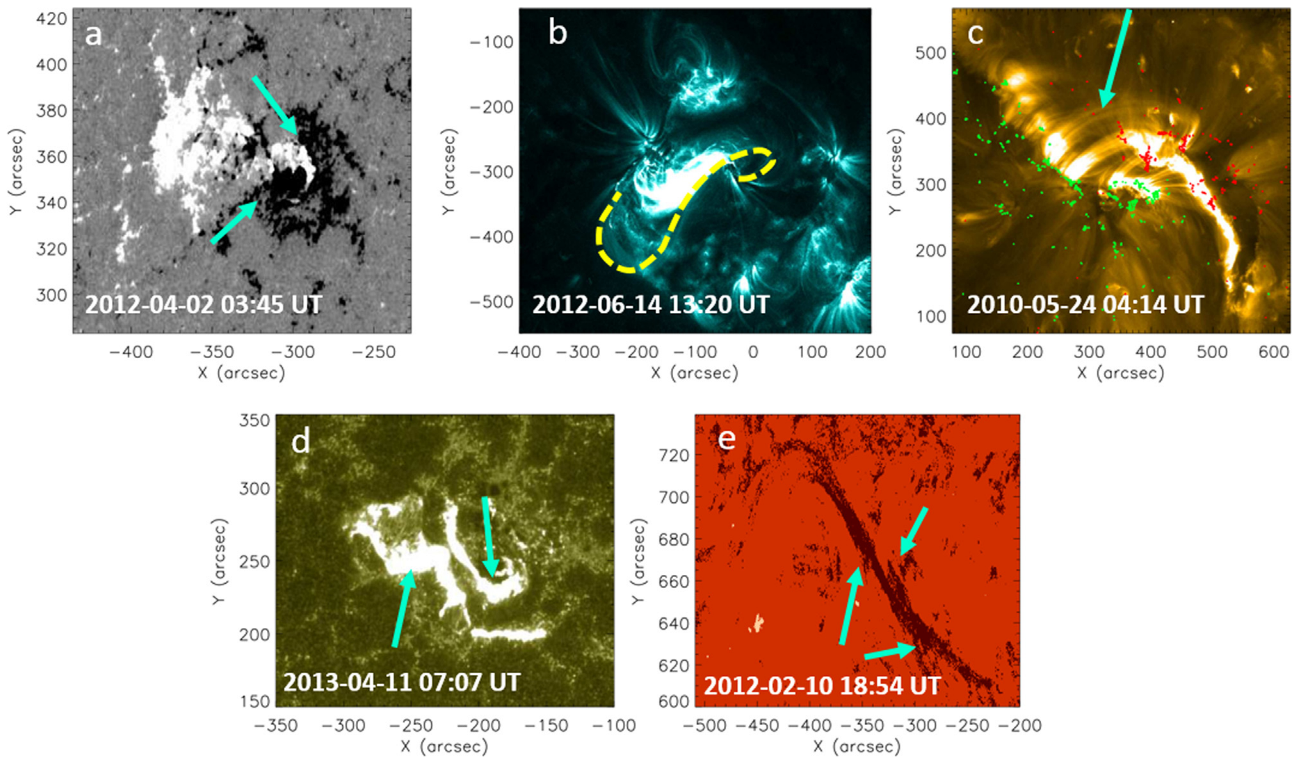

Fig. 2. Magnetogram and EUV proxies for determining chirality of CMEs. (a) Magnetic tongue configuration (indicated using sky-blue arrows on an SDO/HMI LOS magnetogram) associated with right-handed flux tube of Event 5. (b) A forward ‘S’-shaped sigmoid structure (indicated by yellow dashed line on the SDO/AIA 131 Å image) representing a positive twist of Event 6 CME. (c) A left-handed skew of overlying coronal loops (pointed by sky-blue arrow on the SDO/AIA 171 Å image) denoting a negative twist of Event 1 CME. The red and green contours over-plotted on the image refer to negative and positive magnetic field regions with LOS magnetic field intensity $B_{LOS} > \pm 150$ G, respectively. (d) Reverse ‘J’-shaped ribbons pointed by sky-blue arrows on SDO/AIA 1600 Å image. The ribbon structures denote a negative twist of Event 9 CME. (e) A Multi-Scale Gaussian Normalized (MGN; Morgan and Druckmüller, 2014) AIA 304Å image showing the normal-polarity right bearing filament associated with Event 4. The filament associated FR has a positive chirality.

2–3 and 4–5, respectively. In Fig. 3(a) and (b), the scatter plots between H_{cme}-H_{mc} and ϕ_{pcme}-ϕ_{pmc} pairs are shown in logarithmic scale. Three data points with a red square over-plotted on them represent the filament associated events. Others are accompanied by flares. We find a significant positive correlation between H_{cme} and H_{mc} with Pearson correlation coefficient r_p of 0.67 at 97% confidence level. Similar to Qiu et al. (2007), Hu et al. (2014), Gopalswamy et al. (2017), the correlation between ϕ_{pcme} and ϕ_{pmc} are also found to be significant and positive. We perform a quantitative evaluation of flux and helicity relationships in two domains utilizing least-squares fits to the data pairs in logarithmic scale. The dotted lines over-plotted on the plots follow the equation $Y = aX^b$ that best fits the data. The fit equations obtained for helicity and flux pairs for $L_{mc} = 1$ AU are,

$$H_{mc} = (0.5 \pm 0.2) H_{cme}^{0.93 \pm 0.36}, \quad (5)$$

and

$$\phi_{pmc} = (0.8 \pm 0.2) \phi_{pcme}^{0.81 \pm 0.3}, \quad (6)$$

respectively. With the uncertainties, the fitting parameters in Eq. 5 and 6 yield a power-law index b close to unity for both the cases of helicity and flux. On average, the ratio of H_{mc} to H_{cme} is around unity when MC axis length $L_{mc} = 2$ AU. With $L_{mc} = 0.5$ AU as the lower limit of MC axis length, the ratio becomes 0.3 suggesting the total MC helicity being 30% of the CME helicity. With $L_{mc} = 2$ AU, the CME poloidal flux which is equivalent to the reconnection flux contributes 66% to the poloidal flux in MC. The ratio of ϕ_{pmc} to ϕ_{pcme} becomes 0.4 with $L_{mc} = 0.5$ AU. While $L_{mc} = 1$ AU, the MC flux and helicity become less than those transported from sheared arcade to CME FR by low-coronal reconnection. The flux relationship between near-Sun CMEs and 1-AU MCs found in our study is very similar to that found by Qiu et al. (2007). With $L_{mc} = 2.6 \pm 0.3$, the helicity transported to CME during low-coronal reconnection contributes 73–92% to MC helicity. Therefore, within uncertainties these results can be summarized as $H_{mc} \approx H_{cme}$ and $\phi_{pmc} \approx \phi_{pcme}$ that is equivalent to ϕ_{rc}. The results suggest that irrespective of CME association with filament or flare, the flux and helicity transported to CME FRs during low-coronal reconnection are highly relevant to those carried by FRs at 1 AU. We exclude Event 6 from this statistical analysis because of its high rate of flux erosion in interplanetary medium.

4.2. Helicity and flux erosion during Sun-Earth propagation

The presence of relative speed between MC and ambient solar wind plasma causes draping of IMF around MCs and results in magnetic reconnection between MC and oppositely directed draped IMF (McComas et al., 1988) in the interplanetary medium. We apply the direct method described in Section 3.2 to estimate the total poloidal flux ($\phi_{pmc,dir}$) and helicity ($H_{mc,dir}$), where $\phi_{pmc,dir} = \phi_y(x_{be})$ and $H_{mc,dir} = Hel(x_{be})$. We determine the eroded flux $\phi_{pmc,e} = \phi_y(x_{be}) - \phi_y(x_{ae})$ and helicity $H_{mc,e} = Hel(x_{be}) - Hel(x_{ae})$. Dasso et al. (2006) showed that $H_{mc,dir}$ remains in the range of helicity H_{mc} derived from model output. We notice a significant correlation with r_p =0.7 at 99% confidence level between H_{mc} and $H_{mc,dir}$. In Column 6–7 of Table 3, we provide MC's normalised eroded azimuthal flux $\bar{\phi}_{pmc,e}$ and helicity $\overline{H}_{mc,e}$. Here, $\phi_{pmc,e}$ and $H_{mc,e}$ are normalised to $\phi_{pmc,dir}$ and $H_{mc,dir}$. We notice that a high impact parameter (p) value lowers the $\phi_{pmc,dir}$ and $H_{mc,dir}$ estimations which results in an over-estimation of $\bar{\phi}_{pmc,e}$ and $\overline{H}_{mc,e}$. The average normalised $\phi_{pmc,e}$ and $H_{mc,e}$ for the events analysed here are 0.25 and 0.36, respectively. In Column 8, we present the rate of eroded azimuthal flux $Er_{rate} = \frac{\phi_{pmc,e}}{\phi_{pmc}\delta t} \times 100$ during the spacecraft crossing, where the ongoing reconnection starts a lapse of time δt hour (Hr) earlier than the initiation of in situ observation of MC. Column 9 shows Er^{*}_{rate} that represents the rate of normalized eroded flux where FR's axial expansion has been considered while determining its eroded flux. We notice that both Er_{rate} and Er^{*}_{rate} corresponding to Event 6 are comparatively higher than the Er_{rate} and Er^{*}_{rate} of other associated events.

4.3. Comparison of CME and MC Chirality

By careful observations and analyses of CME solar sources using SDO/HMI and AIA instruments, we determine the chirality of CME FRs near the Sun. We locate the chirality proxy signatures discussed in Section 3.3 at CME's solar sources and examine them to infer the CME chirality at the near-Sun domain. It is very unlikely that all chirality proxies can be observed at the source of every single CME. However, hemispheric helicity rule can be applied to each event having well-identified solar sources. A statistical study of Liu et al. (2014) showed that only 60% of FRs follow the hemispheric helicity rule. Table 4 summarises the FR chirality at near-Sun and 1 AU domains. In the first six rows, we provide a summary of near-Sun flux-rope chirality determination. The EUV and magnetogram proxies are mentioned in Column 1, Column 2–12 present the chirality of each event, where '+1' stands for right-handed and '−1' represents left-handed chirality. We use '–' to represent the absence of the corresponding chirality proxy information. We notice that CMEs associated with Events 5 and 8 are determined to be right-handed if magnetic tongue, skew of coronal arcades, and flare ribbon structures are used in chirality determination, whereas the hemispheric helicity rule indicates them to be left-handed FRs. The filament structure associated with Event 4 is observed as a normal-polarity and right-bearing filament in AIA 304 Å image. From the positive magnetic field side, if a filament's barbs are observed to be veered from its axis to the right and if the coronal arcade is observed as right-skewed, the filament is classified as normal-polarity and right-bearing filament (See Fig. 7 of (Chen et al., 2014) for more details). (Guo et al., 2010) found that a normal-polarity and the right-bearing filament has a sinistral (positive) chirality which is opposite from the chirality of an inverse-polarity right-bearing filament. We prefer not to use the hemispheric helicity rule for CMEs associated with Events 4, 5, and 8 to determine their chirality. We determine the chirality of MCs using both MVA and linear force-free FRF methods. Row 7 and 8 of Table 4 describes the MC chirality determined using FRF and MVA, respectively. It is noticed that for each event studied here, the chirality of CMEs obtained at the source matches those of MCs derived at 1 AU.

Table 3
Magnetic properties of near-Sun (at 10 R_s) and near-Earth (at 1 AU) FRs along with the erosion rate of FR poloidal flux.

Ev No. (1)	$\phi_{pcme} \pm \delta_{\phi_{pcme}}$ (10^{21}Mx) (2)	$H_{cme} \pm \delta_{H_{cme}}$ (10^{42}Mx^2) (3)	ϕ_{pmc}/L_{mc} (10^{21}Mx/AU) (4)	H_{mc}/L_{mc} (10^{42}Mx^2/AU) (5)	$\bar{\phi}_{pmc,e}$ (6)	$\overline{H}_{mc,e}$ (7)	Er_{rate} (%/Hr) (8)	Er^{*}_{rate} (%/Hr) (9)
1	2.15±0.2	1.9±0.5	1.43	0.67	0.14	0.26	1.46	1.46
2	1.1±0.12	0.37±0.12	0.8	0.21	0.6	0.76	1.76	2.1
3	1.8±0.26	1±0.4	0.92	0.12	0.23	0.35	0.3	0.3
4	2±0.3	1.8±0.7	1.32	1.07	0.69	0.86	1.25	1.6
5	3±0.18	4±0.7	1.13	0.36	0.14	0.31	0.19	0.19
6	8±0.36	26.4±0.4	3.3	2.7	0.11	0.15	3.68	4.6
7	2.5±0.35	2.4±0.9	2.4	2.5	0.09	0.13	0.12	0.12
8	4±0.28	8.5±2	2.41	3	0.57	0.2	0.72	0.74
9	3.7±0.44	6.3±2	2.71	3.85	0.57	0.78	0.34	0.34
10	1.5±0.12	1.3±0.3	2.34	3.93	0.11	0.05	0.18	0.18
11	3.5±0.2	7.8±1.4	3	6.42	0.06	0.09	0.28	0.28

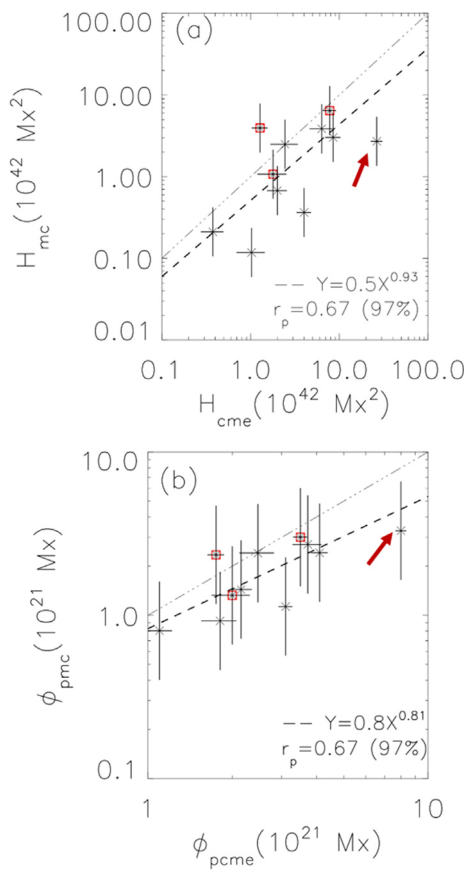

Fig. 3. Scatter plots between (a) helicity of CMEs (H_{cme}) versus MCs (H_{mc}) and poloidal flux of CMEs (ϕ_{pcme}) versus MCs (ϕ_{pmc}) in logarithmic scale. The over-plotted dashed lines represent the least-squares fits to the data. The dashed-dotted lines in both plots show $H_{cme} = H_{mc}$ and $\phi_{pcme} = \phi_{pmc}$ lines, respectively. The asterisk symbols inside red squares represent filament associated events. The red arrows indicate the data point corresponds to Event 6 that is not included in statistical analysis. The fit equations along with correlation coefficient (r_p) values are mentioned on the plots.

5. Discussion

This work investigates the process that transports magnetic helicity and flux in the interplanetary medium during eruptions. There is very little doubt that magnetic reconnection is essential to release FRs during solar eruptions (Antiochos et al., 1999). With eleven solar eruptive events, we investigate FR's helicity and flux conservation properties to understand twisted FR formations and how to transfer magnetic properties in FRs during eruptions. Out of eleven, three events are accompanied by filaments, and rests are associated with flares. We find consistency in twisted flux and helicity of FRs between near-Sun and near-Earth domains for ten out of eleven events, while the magnetic properties of CMEs at source are calculated using post-eruption arcades (PEAs). This result has no dependency on accompanied phenomena like flares and filaments.

We notice that by employing direct method only the lower limit of eroded flux and helicity can be obtained because part of MC's reconnected field lines may completely detach from it before applying the method in situ observation. The total flux and helicity calculated using the direct method can be underestimated if the impact parameter has a high-value (Ruffenach et al., 2015; Pal et al., 2020). Therefore, in the statistical analysis performed in Section 4.1, we utilize model-derived total flux and helicity values.

Determination of a correct FR axis orientation is required in the direct method. As the root mean square error E_{rms} in fitting model to MCs is higher than 0.3 (where Marubashi and Lepping (2007) adopted $E_{rms} < 0.3$ as a criteria for the good agreement between observed and model fit results) for Event 2, 4 and 10, we apply MVA to find their FR axis orientations. By peeling off CME's envelop, erosion may substantially reduce CME poloidal flux and helicity, and lead inconsistency in CME intrinsic properties between near-Sun and near-Earth domains. We notice that by including Event 6 in our statistical analysis, the values of correlation coefficient that is used to find the relevance in CME poloidal flux and helicity between near the Sun and 1 AU, significantly decrease. This happens mostly because of its high rate of erosion (see Column 8 and 9 of Table 3). Cassak and Shay (2007) and Nakamura et al. (2018) showed that the rate of magnetic reconnection causing erosion depends on the magnetic field intensity and velocity of either side of the inflow regions of magnetic reconnection. Therefore, an interplanetary FR with high magnetic field intensity and/or high speed may have a high reconnection rate with the interplanetary field lines draping about them. We notice that the FR axial field intensity (B_{mc}) of Event 6 is ≈ 2.6 times greater than the average $B_{mc} = 18.6$ nT found for the rest of the events, which explains the reason behind a comparatively higher erosion rate of Event 6 than that of the others. In our study, the chirality, which refers to the sense of twist of FRs, is found to be unchanged while FRs propagate from the Sun to the Earth. Here, we utilize the combination of six indirect chirality proxies to obtain FR chirality at their sources. At 1 AU, we use both cylindrical model and MVA methods to find the FR chirality. Palmerio et al. (2018) studied and compared the type, i.e., the orientation and handedness of twenty FRs at their source and 1 AU, and found that although rotation of FRs can change their types, the FR chirality remains unchanged while propagating from Sun to Earth. Our result implies that although magnetic reconnection at solar sources has a significant contribution in forming twisted FRs, the chirality of FRs remains unchanged during this process. The FR chirality being similar to that of its source region conforms to the fact that during reconnection helicity is conserved (Berger, 2005).

6. Summary and conclusions

This statistical study compares the magnetic properties, specifically magnetic helicity and flux in interplanetary CME flux ropes at 1 AU and those contributing via low

Table 4
Chirality determination of near-Sun and near-Earth FRs.

#	Chirality Proxy (1)	Ev 1 (2)	Ev 2 (3)	Ev 3 (4)	Ev 4 (5)	Ev 5 (6)	Ev 6 (7)	Ev 7 (8)	Ev 8 (9)	Ev 9 (10)	Ev 10 (11)	Ev 11 (12)
1	Magnetic tongues	–	–	–	–	+1	+1	–	+1	–	–	–
2	Dextral and sinistral natures of filament structures	–	–	+1	+1	–	–	–	–	-1	-1	–
3	EUV sigmoids	-1	+1	+1	–	–	+1	+1	–	-1	–	-1
4	Skew of coronal arcades overlying the neutral lines	–	–	+1	–	+1	+1	+1	+1	-1	–	-1
5	Structure of flare-ribbons	−1	–	–	–	–	–	–	+1	−1	−1	–
6	Hemispheric helicity rule	−1	+1	+1	−1	−1	+1	+1	−1	−1	−1	−1
7	FRF	−1	+1	+1	+1	+1	+1	+1	+1	−1	−1	−1
8	MVA	−1	+1	+1	+1	+1	+1	+1	+1	−1	−1	−1

coronal magnetic reconnection at progenitor sheared magnetic arcades. We assume FRs as force-free cylindrical structures whose helicity and flux depend on their magnetic field strength, cross-sectional radius, and axial length. At 1 AU, these parameters are estimated by fitting a linear force-free cylindrical model to FRs. Near the Sun, at 10 R_s, the parameters are derived by combining low-coronal reconnection flux with FR physical parameters estimated by forward modeling the FRs. Within the uncertainty range, the helicity and poloidal flux in FRs at 1 AU are highly relevant with those contributing during low coronal reconnection, irrespective of FR associations with flares and/or filaments. Moreover, if the length of MCs is 2 AU, the ratio of FR helicity at source and 1 AU becomes almost unity. By analyzing the erosion in FR helicity resulted from reconnection with IMFs, it is noticed that a high rate of erosion in the interplanetary medium may significantly lower the helicity in FRs during Sun-Earth propagation. This work addresses a quantitative relationship between magnetic helicity and flux budgets in low-corona reconnection and interplanetary FRs. The result uses eleven events that constitute a reasonable statistical sample to provide a better idea of the context of twisted eruptive FR formations and the process that mainly allows the transportation of solar flux and helicity into the heliosphere via eruptive FRs appearing as CMEs at low corona and MCs at 1 AU. The knowledge of eruptive FR formations and the source of their geoeffectiveness determined by their magnetic structure may eventually lead to a better forecast and assessment of space weather.

Declaration of Competing Interest

The authors declare the following financial interests/personal relationships which may be considered as potential competing interests: [The author Dr. Sanchita Pal, hereby declares that part of this work is partially supported by the Center of Excellence in Space Sciences India (CESSI) that is funded by the Ministry of Human Resource Development, Government of India under the Frontier Areas of Science and Technology scheme.]

Acknowledgments

This work is partially supported by the Center of Excellence in Space Sciences India (CESSI) that is funded by the Ministry of Human Resource Development, Government of India under the Frontier Areas of Science and Technology scheme. The author is grateful to Dr. Katsuhide Marubashi for making available the linear force free cylindrical flux rope model. The author is thankful to Prof. Dibyendu Nandy for his help in improving the quality of this work. The author thanks the referees for their helpful comments and suggestions that improve the manuscript. The author acknowledges the use of data from the SDO, SOHO, STEREO and ACE instruments.

References

Antiochos, S., DeVore, C., Klimchuk, J., 1999. A model for solar coronal mass ejections. Astrophys. J. 510 (1), 485.

Berger, M.A., 2003. Topological quantities in magnetohydrodynamics. In: Ferriz-Mas, A., Núñez, M. (Eds.), Advances in Nonlinear Dynamics. CRC Press, London, pp. 345–374. https://doi.org/10.1201/9780203493137.ch10.

Berger, M.A., 2005. Magnetic Helicity Conservation. Highlights Astron. 13, 85.

Berger, M.A., Field, G.B., 1984. The topological properties of magnetic helicity. J. Fluid Mech. 147, 133–148.

Bothmer, V., Rust, D., 1997. In: Crooker, N., Ja Joselyn, Feynman, J. (Eds.), Coronal Mass Ejections, pp. 139–146.

Bothmer, V., Schwenn, R., 1998. The structure and origin of magnetic clouds in the solar wind. Ann. Geophys. 16 (1), 1–24. https://doi.org/10.1007/s00585-997-0001-x, URL https://www.ann-geophys.net/16/1/1998/.

Brueckner, G., Howard, R., Koomen, M., Korendyke, C., Michels, D., Moses, J., Socker, D., Dere, K., Lamy, P., Llebaria, A., et al., 1995. The large angle spectroscopic coronagraph (lasco). In: The SOHO Mission. Springer, pp. 357–402.

Burlaga, L., Plunkett, S., St. Cyr, O., 2002. Successive cmes and complex ejecta. J. Geophys. Res.: Space Phys. 107 (A10), SSH-1.

Burlaga, L., Sittler, E., Mariani, F., Schwenn, R., 1981. Magnetic loop behind an interplanetary shock: Voyager, helios, and imp 8 observations. J. Geophys. Res. (Space Phys.) 86 (A8), 6673–6684. https://doi.org/10.1029/JA086iA08p06673.

Cane, H., Richardson, I., Wibberenz, G., 1997. Helios 1 and 2 observations of particle decreases, ejecta, and magnetic clouds. J. Geophys. Res.: Space Phys. 102 (A4), 7075–7086.

Canfield, R.C., Hudson, H.S., McKenzie, D.E., 1999. Sigmoidal morphology and eruptive solar activity. Geophys. Res. Lett. 26 (6), 627–630.

Cassak, P., Shay, M., 2007. Scaling of asymmetric magnetic reconnection: General theory and collisional simulations. Phys. Plasmas 14 (10), 102114.

Chen, P., Harra, L., Fang, C., 2014. Imaging and spectroscopic observations of a filament channel and the implications for the nature of counter-streamings. Astrophys. J. 784 (1), 50.

Cho, K.S., Moon, Y.J., Dryer, M., Fry, C.D., Park, Y.D., Kim, K.S., 2003. A statistical comparison of interplanetary shock and CME propagation models. J. Geophys. Res. (Space Phys.) 108 (A12), 1445. https://doi.org/10.1029/2003JA010029.

Choe, G., Cheng, C., 2000. A model of solar flares and their homologous behavior. Astrophys. J. 541 (1), 449.

Crooker, N., 2000. Solar and heliospheric geoeffective disturbances. J. Atmos. Solar Terr. Phys. 62 (12), 1071–1085.

Dasso, S., Mandrini, C.H., DéMoulin, P., Farrugia, C.J., 2003. Magnetic helicity analysis of an interplanetary twisted flux tube. J. Geophys. Res. (Space Phys.) 108 (A10), 1362. https://doi.org/10.1029/2003JA009942.

Dasso, S., Mandrini, C.H., Démoulin, P., Luoni, M.L., 2006. A new model-independent method to compute magnetic helicity in magnetic clouds. Astron. Astrophys. 455, 349–359. https://doi.org/10.1051/0004-6361:20064806.

Dasso, S., Mandrini, C.H., Luoni, M.L., Gulisano, A.M., Nakwacki, M. S., Pohjolainen, S., van Driel-Gesztelyi, L., Démoulin, P., 2005. Linking coronal to heliospheric magnetic helicity: A new model-independent technique to compute helicity in magnetic clouds. In: Solar Wind 11/SOHO 16, Connecting Sun and Heliosphere, vol. 592, p. 605.

Dasso, S., Nakwacki, M., Démoulin, P., Mandrini, C., 2007. Progressive transformation of a flux rope to an icme. Sol. Phys. 244 (1), 115–137.

Démoulin, P., Janvier, M., Dasso, S., 2016. Magnetic flux and helicity of magnetic clouds. Sol. Phys. 291 (2), 531–557.

Démoulin, P., Mandrini, C.H., van Driel-Gesztelyi, L., Thompson, B., Plunkett, S., Kővári, Z., Aulanier, G., Young, A., 2002. What is the source of the magnetic helicity shed by cmes? the long-term helicity budget of ar 7978. Astron. Astrophys. 382 (2), 650–665.

Démoulin, P., Priest, E., Lonie, D., 1996. Three-dimensional magnetic reconnection without null points: 2. application to twisted flux tubes. J. Geophys. Res. (Space Phys.) 101 (A4), 7631–7646.

Dere, K., Brueckner, G., Howard, R., Michels, D., Delaboudiniere, J., 1999. Lasco and eit observations of helical structure in coronal mass ejections. Astrophys. J. 516 (1), 465.

DeVore, C.R., 2000. Magnetic helicity generation by solar differential rotation. Astrophys. J. 539 (2), 944.

Domingo, V., Fleck, B., Poland, A.I., 1995. The soho mission: an overview. Sol. Phys. 162 (1), 1–37.

Fan, Y., Gibson, S., 2004. Numerical simulations of three-dimensional coronal magnetic fields resulting from the emergence of twisted magnetic flux tubes. Astrophys. J. 609 (2), 1123.

Forbes, T., Priest, E., 1995. Photospheric magnetic field evolution and eruptive flares. Astrophys. J. 446, 377.

Fuentes, M.L., Démoulin, P., Mandrini, C.H., van Driel-Gesztelyi, L., 2000. The counterkink rotation of a non-hale active region. Astrophys. J. 544 (1), 540.

Georgoulis, M.K., Nindos, A., Zhang, H., 2019. The source and engine of coronal mass ejections. Philosoph. Trans. Roy. Soc. A 377 (2148), 20180094.

Gopalswamy, N., Akiyama, S., Yashiro, S., Xie, H., 2017. A new technique to provide realistic input to cme forecasting models. Proc. Int. Astron. Union 13 (S335), 258–262.

Gopalswamy, N., Yashiro, S., Akiyama, S., Xie, H., 2017. Estimation of reconnection flux using post-eruption arcades and its relevance to magnetic clouds at 1 au. Sol. Phys. 292 (4), 65.

Guo, Y., Schmieder, B., Démoulin, P., Wiegelmann, T., Aulanier, G., Török, T., Bommier, V., 2010. Coexisting flux rope and dipped arcade sections along one solar filament. Astrophys. J. 714 (1), 343.

Howard, R.A., Moses, J., Vourlidas, A., Newmark, J., Socker, D.G., Plunkett, S.P., Korendyke, C.M., Cook, J., Hurley, A., Davila, J., et al., 2008. Sun earth connection coronal and heliospheric investigation (secchi). Space Sci. Rev. 136 (1), 67–115.

Hu, Q., Qiu, J., Dasgupta, B., Khare, A., Webb, G., 2014. Structures of interplanetary magnetic flux ropes and comparison with their solar sources. Astrophys. J. 793 (1), 53.

Kaiser, M.L., Kucera, T., Davila, J., Cyr, O.S., Guhathakurta, M., Christian, E., 2008. The stereo mission: An introduction. Space Sci. Rev. 136 (1), 5–16.

Kilpua, E., Jian, L., Li, Y., Luhmann, J., Russell, C., 2011. Multipoint icme encounters: Pre-stereo and stereo observations. J. Atmos. Solar Terr. Phys. 73 (10), 1228–1241.

Larson, D., Lin, R., McTiernan, J., McFadden, J., Ergun, R., McCarthy, M., Reme, H., Sanderson, T., Kaiser, M., Lepping, R., et al., 1997. Tracing the topology of the october 18–20, 1995, magnetic cloud with $0.1–10^2$ kev electrons. Geophys. Res. Lett. 24 (15), 1911–1914.

Leamon, R.J., Canfield, R.C., Jones, S.L., Lambkin, K., Lundberg, B.J., Pevtsov, A.A., 2004. Helicity of magnetic clouds and their associated active regions. J. Geophys. Res.: Space Phys. 109 (A5).

Lemen, J.R., Akin, D.J., Boerner, P.F., Chou, C., Drake, J.F., Duncan, D.W., Edwards, C.G., Friedlaender, F.M., Heyman, G.F., Hurlburt, N.E., et al., 2011. The atmospheric imaging assembly (aia) on the solar dynamics observatory (sdo). In: The Solar Dynamics Observatory. Springer, pp. 17–40.

Lepping, R., Burlaga, L., Szabo, A., Ogilvie, K., Mish, W., Vassiliadis, D., Lazarus, A., Steinberg, J., Farrugia, C., Janoo, L., et al., 1997. The wind magnetic cloud and events of october 18–20, 1995: Interplanetary properties and as triggers for geomagnetic activity. J. Geophys. Res.: Space Phys. 102 (A7), 14049–14063.

Lepping, R.P., Burlaga, L.F., Jones, J.A., 1990. Magnetic field structure of interplanetary magnetic clouds at 1 AU. J. Geophys. Res. 95, 11957–11965. https://doi.org/10.1029/JA095iA08p11957.

Lin, J., Raymond, J., Van Ballegooijen, A., 2004. The role of magnetic reconnection in the observable features of solar eruptions. Astrophys. J. 602 (1), 422.

Liu, Y., Hoeksema, J., Bobra, M., Hayashi, K., Schuck, P., Sun, X., 2014. Magnetic helicity in emerging solar active regions. Astrophys. J. 785 (1), 13.

Longcope, D., Beveridge, C., 2007. A quantitative, topological model of reconnection and flux rope formation in a two-ribbon flare. Astrophys. J. 669 (1), 621.

Low, B., 1994. Magnetohydrodynamic processes in the solar corona: Flares, coronal mass ejections, and magnetic helicity. Phys. Plasmas 1 (5), 1684–1690.

Low, B., 1996. Solar activity and the corona. Sol. Phys. 167 (1), 217–265.

Luoni, M.L., Démoulin, P., Mandrini, C.H., van Driel-Gesztelyi, L., 2011. Twisted flux tube emergence evidenced in longitudinal magnetograms: magnetic tongues. Sol. Phys. 270 (1), 45.

Lynch, B., Antiochos, S., MacNeice, P., Zurbuchen, T., Fisk, L., 2004. Observable properties of the breakout model for coronal mass ejections. Astrophys. J. 617 (1), 589.

Mackay, D., Van Ballegooijen, A., 2001. A possible solar cycle dependence to the hemispheric pattern of filament magnetic fields? Astrophys. J. 560 (1), 445.

Manchester, W., Kilpua, E.K., Liu, Y.D., Lugaz, N., Riley, P., Török, T., Vršnak, B., 2017. The physical processes of cme/icme evolution. Space Sci. Rev. 212 (3), 1159–1219.

Mandrini, C.H., Pohjolainen, S., Dasso, S., Green, L., Démoulin, P., van Driel-Gesztelyi, L., Copperwheat, C., Foley, C., 2005. Interplanetary flux rope ejected from an x-ray bright point-the smallest magnetic cloud source-region ever observed. Astron. Astrophys. 434 (2), 725–740.

Martin, S., McAllister, A., 1996. The skew of x-ray coronal loops overlying hαfilaments. In: Magnetodynamic Phenomena in the Solar Atmosphere. Springer, pp. 497–498.
Martin, S., McAllister, A., 1997. Predicting the sign of magnetic helicity in erupting filaments and coronal mass ejections. Washington DC Am. Geophys. Union Geophys. Monograph Series 99, 127–138.
Martin, S.F., 1998. Filament chirality: A link between fine-scale and global patterns. In: International Astronomical Union Colloquium. vol. 167, Cambridge University Press. pp. 419–429.
Martin, S.F., 2003. Signs of helicity in solar prominences and related features. Adv. Space Res. 32 (10), 1883–1893.
Marubashi, K., 1986. Structure of the interplanetary magnetic clouds and their solar origins. Adv. Space Res. 6 (6), 335–338. https://doi.org/10.1016/0273-1177(86)90172-9.
Marubashi, K., Lepping, R.P., 2007. Long-duration magnetic clouds: a comparison of analyses using torus- and cylinder-shaped flux rope models. Ann. Geophys. 25 (11), 2453–2477. https://doi.org/10.5194/angeo-25-2453-2007.
McAllister, A., Hundhausen, A., Burkpile, J., McIntosh, P., Hiei, E., 1995. Declining phase coronal evolution: The statistics of x-ray arcades. In: Bulletin of the American Astronomical Society, vol. 27, p. 961.
McAllister, A.H., Dryer, M., McIntosh, P., Singer, H., Weiss, L., 1996. A large polar crown coronal mass ejection and a "problem" geomagnetic storm: April 14–23, 1994. J. Geophys. Res. 101 (A6), 13497–13516. https://doi.org/10.1029/96JA00510.
McAllister, A.H., Martin, S.F., Crooker, N.U., Lepping, R.P., Fitzenreiter, R.J., 2001. A test of real-time prediction of magnetic cloud topology and geomagnetic storm occurrence from solar signatures. J. Geophys. Res. 106 (A12), 29185–29194. https://doi.org/10.1029/2000JA000032.
McCauley, P.I., Su, Y.N., Schanche, N., Evans, K.E., Su, C., McKillop, S., Reeves, K.K., 2015. Prominence and Filament Eruptions Observed by the Solar Dynamics Observatory: Statistical Properties, Kinematics, and Online Catalog. Sol. Phys. 290 (6), 1703–1740. https://doi.org/10.1007/s11207-015-0699-7, arXiv:1505.02090.
McComas, D., Gosling, J., Winterhalter, D., Smith, E., 1988. Interplanetary magnetic field draping about fast coronal mass ejecta in the outer heliosphere. J. Geophys. Res.: Space Phys. 93 (A4), 2519–2526.
McComas, D.J., Bame, S.J., Barker, P., Feldman, W.C., Phillips, J.L., Riley, P., Griffee, J.W., 1998. Solar Wind Electron Proton Alpha Monitor (SWEPAM) for the Advanced Composition Explorer. Space Sci. Rev. 86, 563–612. https://doi.org/10.1023/A:1005040232597.
Moore, R., Labonte, B., 1980. Solar and interplanetary dynamics. In: IAU Symp. D. Reidel Boston, USA vol. 91, p. 207.
Morgan, H., Druckmüller, M., 2014. Multi-Scale Gaussian Normalization for Solar Image Processing. Sol. Phys. 289 (8), 2945–2955. https://doi.org/10.1007/s11207-014-0523-9, arXiv:1403.6613.
Mulligan, T., Russell, C.T., Luhmann, J.G., 1998. Solar cycle evolution of the structure of magnetic clouds in the inner heliosphere. Geophys. Res. Lett. 25 (15), 2959–2962. https://doi.org/10.1029/98GL01302.
Nakamura, T.K., Genestreti, K., Liu, Y.-H., Nakamura, R., Teh, W.-L., Hasegawa, H., Daughton, W., Hesse, M., Torbert, R., Burch, J., et al., 2018. Measurement of the magnetic reconnection rate in the earth's magnetotail. J. Geophys. Res.: Space Phys. 123 (11), 9150–9168.
Nandy, D., 2006. Magnetic helicity and flux tube dynamics in the solar convection zone: Comparisons between observation and theory. J. Geophys. Res. (Space Phys.) 111 (A12), A12S01. https://doi.org/10.1029/2006JA011882.
Nindos, A., Zhang, H., 2002. Photospheric motions and coronal mass ejection productivity. Astrophys. J. Lett. 573 (2), L133.
Nindos, A., Zhang, J., Zhang, H., 2003. The magnetic helicity budget of solar active regions and coronal mass ejections. Astrophys. J. 594 (2), 1033.
Odstrcil, D., Pizzo, V.J., 1999. Distortion of the interplanetary magnetic field by three-dimensional propagation of coronal mass ejections in a structured solar wind. J. Geophys. Res.: Space Phys. 104 (A12), 28225–28239.
Pal, S., Dash, S., Nandy, D., 2020. Flux Erosion of Magnetic Clouds by Reconnection With the Sun's Open. Flux. 47 (8), e86372. https://doi.org/10.1029/2019GL086372, arXiv:2103.05990.
Pal, S., Gopalswamy, N., Nandy, D., Akiyama, S., Yashiro, S., Makela, P., Xie, H., 2017. A Sun-to-Earth Analysis of Magnetic Helicity of the 2013 March 17–18 Interplanetary Coronal Mass Ejection. Astrophys. J. 851 (2), 123. https://doi.org/10.3847/1538-4357/aa9983, arXiv:1712.01114.
Pal, S., Kilpua, Emilia, Good, Simon, Pomoell, Jens, Price, Daniel J., 2021. Uncovering erosion effects on magnetic flux rope twist. A&A 650, A176. https://doi.org/10.1051/0004-6361/202040070.
Pal, S., Nandy, D., Srivastava, N., Gopalswamy, N., Panda, S., 2018. Dependence of coronal mass ejection properties on their solar source active region characteristics and associated flare reconnection flux. Astrophys. J. 865 (1), 4.
Palmerio, E., Kilpua, E.K., James, A.W., Green, L.M., Pomoell, J., Isavnin, A., Valori, G., 2017. Determining the intrinsic cme flux rope type using remote-sensing solar disk observations. Sol. Phys. 292 (2), 39.
Palmerio, E., Kilpua, E.K., Möstl, C., Bothmer, V., James, A.W., Green, L.M., Isavnin, A., Davies, J.A., Harrison, R.A., 2018. Coronal magnetic structure of earthbound cmes and in situ comparison. Space Weather 16 (5), 442–460.
Patsourakos, S., Vourlidas, A., Török, T., Kliem, B., Antiochos, S., Archontis, V., Aulanier, G., Cheng, X., Chintzoglou, G., Georgoulis, M., et al., 2020. Decoding the pre-eruptive magnetic field configurations of coronal mass ejections. Space Sci. Rev. 216 (8), 1–63.
Pesnell, W.D., Thompson, B.J., Chamberlin, P., 2011. The solar dynamics observatory (sdo). In: The Solar Dynamics Observatory. Springer, pp. 3–15.
Pevtsov, A., Balasubramaniam, K., 2003. Helicity patterns on the sun. Adv. Space Res. 32 (10), 1867–1874.
Pevtsov, A.A., Berger, M.A., Nindos, A., Norton, A.A., van Driel-Gesztelyi, L., 2014. Magnetic helicity, tilt, and twist. Space Sci. Rev. 186 (1–4), 285–324.
Qiu, J., Hu, Q., Howard, T.A., Yurchyshyn, V.B., 2007. On the Magnetic Flux Budget in Low-Corona Magnetic Reconnection and Interplanetary Coronal Mass Ejections. Astrophys. J. 659, 758–772. https://doi.org/10.1086/512060.
Richardson, I.G., Cane, H.V., 2010. Near-earth interplanetary coronal mass ejections during solar cycle 23 (1996–2009): Catalog and summary of properties. Sol. Phys. 264 (1), 189–237. https://doi.org/10.1007/s11207-010-9568-6.
Ruffenach, A., Lavraud, B., Farrugia, C.J., Démoulin, P., Dasso, S., Owens, M.J., Sauvaud, J.-A., Rouillard, A., Lynnyk, A., Foullon, C., et al., 2015. Statistical study of magnetic cloud erosion by magnetic reconnection. J. Geophys. Res.: Space Phys. 120 (1), 43–60.
Ruffenach, A., Lavraud, B., Owens, M.J., Sauvaud, J.-A., Savani, N.P., Rouillard, A.P., Démoulin, P., Foullon, C., Opitz, A., Fedorov, A., Jacquey, C.J., Génot, V., Louarn, P., Luhmann, J.G., Russell, C.T., Farrugia, C.J., Galvin, A.B., 2012. Multispacecraft observation of magnetic cloud erosion by magnetic reconnection during propagation. J. Geophys. Res. (Space Phys.) 117, A09101. https://doi.org/10.1029/2012JA017624.
Rust, D., Kumar, A., 1996. Evidence for helically kinked magnetic flux ropes in solar eruptions astrophys. J 464, L199–L202.
Rust, D.M., 1983. Coronal disturbances and their terrestrial effects. Space Sci. Rev. 34 (1), 21–36.
Sarkar, R., Gopalswamy, N., Srivastava, N., 2020. An observationally constrained analytical model for predicting the magnetic field vectors of interplanetary coronal mass ejections at 1 au. Astrophys. J. 888 (2), 121.
Savani, N.P., Owens, M.J., Rouillard, A.P., Forsyth, R.J., Davies, J.A., 2010. Observational Evidence of a Coronal Mass Ejection Distortion Directly Attributable to a Structured Solar Wind. Astrophys. Phys. J. Lett. 714 (1), L128–L132. https://doi.org/10.1088/2041-8205/714/1/L128.

Scherrer, P.H., Schou, J., Bush, R., Kosovichev, A., Bogart, R., Hoeksema, J., Liu, Y., Duvall, T., Zhao, J., Schrijver, C., et al., 2012. The helioseismic and magnetic imager (hmi) investigation for the solar dynamics observatory (sdo). Sol. Phys. 275 (1), 207–227.

Schmieder, B., Aulanier, G., Vršnak, B., 2015. Flare-cme models: an observational perspective (invited review). Sol. Phys. 290 (12), 3457–3486.

Smith, C.W., L'Heureux, J., Ness, N.F., Acuña, M.H., Burlaga, L.F., Scheifele, J., 1998. The ACE Magnetic Fields Experiment. Space Sci. Rev. 86, 613–632. https://doi.org/10.1023/A:1005092216668.

Sonnerup, B.Ö., Cahill Jr, L., 1967. Magnetopause structure and attitude from explorer 12 observations. J. Geophys. Res. 72 (1), 171–183.

Sterling, A.C., Hudson, H.S., 1997. Yohkoh sxt observations of x-ray "dimming" associated with a halo coronal mass ejection. Astrophys. J. Lett. 491 (1), L55.

Sturrock, P.A., 1989. The role of eruption in solar flares. International Astronomical Union Colloquium, vol. 104. Cambridge University Press, pp. 387–397.

Thernisien, A.F.R., Howard, R.A., Vourlidas, A., 2006. Modeling of Flux Rope Coronal Mass Ejections. Astrophys. J. 652, 763–773. https://doi.org/10.1086/508254.

Titov, V., Démoulin, P., 1999. Basic topology of twisted magnetic configurations in solar flares. Astron. Astrophys. 351, 707–720.

Tripathi, D., Bothmer, V., Cremades, H., 2004. The basic characteristics of EUV post-eruptive arcades and their role as tracers of coronal mass ejection source regions. Astron. Astrophys. 422, 337–349. https://doi.org/10.1051/0004-6361:20035815.

Vourlidas, A., Lynch, B.J., Howard, R.A., Li, Y., 2013. How many cmes have flux ropes? deciphering the signatures of shocks, flux ropes, and prominences in coronagraph observations of cmes. Sol. Phys. 284 (1), 179–201.

Webb, D., Lepping, R., Burlaga, L., DeForest, C., Larson, D., Martin, S., Plunkett, S., Rust, D., 2000. The origin and development of the May 1997 magnetic cloud. J. Geophys. Res.: Space Phys. 105 (A12), 27251–27259.

Webb, D.F., Howard, T.A., 2012. Coronal mass ejections: Observations. Living Rev. Sol. Phys. 9 (1), 1–83.

Winslow, R.M., Lugaz, N., Schwadron, N.A., Farrugia, C.J., Yu, W., Raines, J.M., Mays, M.L., Galvin, A.B., Zurbuchen, T.H., 2016. Longitudinal conjunction between messenger and stereo a: Development of icme complexity through stream interactions. J. Geophys. Res.: Space Phys. 121 (7), 6092–6106.

Woltjer, L., 1958. On hydromagnetic equilibrium. Proc. National Acad. Sci. USA 44 (9), 833.

Youssef, M., Mawad, R., et al., 2013. A statistical study of post-flare-associated cme events. Adv. Space Res. 51 (7), 1221–1229.

Zhang, J., Richardson, I.G., Webb, D.F., Gopalswamy, N., Huttunen, E., Kasper, J., Nitta, N.V., Poomvises, W., Thompson, B.J., Wu, C.-C., Yashiro, S., Zhukov, A.N., 2007. Correction to "solar and interplanetary sources of major geomagnetic storms (dst <= -100 nt) during 1996–2005". J. Geophys. Res. (Space Phys.) 112, A12103. https://doi.org/10.1029/2007JA012891.